DOI: 10.37190/ ABB-02338-2023-03

Study on Glass Forming Ability and Corrosion Performance of Ca Based Biomedical Materials

Jing Feng[1], Yue Wang[1], Dehua Liu[1], Yong Zhang[2], Guihong Geng[1]*

[1] School of Materials Science and Engineering, North Minzu University, Yinchuan 750021, P.R. China

[2] State Key Laboratory for Advanced Metals and Materials, University of Science and Technology Beijing, Beijing 100083, China.

*Corresponding author: Guihong Geng, School of Materials Science and Engineering, North Minzu University, Yinchuan 750021, P.R. China, e-mail address: gengguihong@nmu.edu.cn

Submitted: 2nd November 2023

Accepted: 10th February 2024

Abstract

Stress shielding and the need for secondary surgery are the two major challenges faced by permanent metallic implants, and the emerging Ca-Mg-Zn calcium-based bulk amorphous alloys, with Young's modulus comparable to that of human bone, good biocompatibility, and in vivo degradation, are highly promising materials for bioimplants. Few studies have been reported on the glass formation ability (GFA) and corrosion degradation behavior of Ca-Mg-Zn amorphous alloys in the human body. In this work, we discuss a study on $Ca_{53+x}Mg_{20}Zn_{27-x}$(x=0,2,4,6,8,10) alloys, focusing on changes in Zn content near eutectic points and their impact on microstructure and biological corrosion behavior. A copper mold spray casting method has been developed to prepare amorphous bar alloys and amorphous crystalline composite bar alloys with a diameter of 3 mm, which has been verified by X-ray diffraction, electrochemical treatment, and immersion tests. The experimental results demonstrated that the Ca_3Zn and $CaZn_2$ phases were precipitated in the 3mm bar material $Ca_{53+x}Mg_{20}Zn_{27-x}$ (x = 0, 2, 4), and $Ca_{53+x}Mg_{20}Zn_{27-x}$ (x = 6, 8, 10) was completely amorphous. The $Ca_{63}Mg_{20}Zn_{17}$ alloy showed the best glass-forming ability, while the $Ca_{59}Mg_{20}Zn_{21}$ alloy exhibited superior corrosion resistance. Cytotoxicity experiments showed that Ca-Mg-Zn alloys have good biocompatibility and can be used as biomedical materials.

Key words: Metallic glasses; Microstructure; Corrosion; Crystallization

1. Introduction

Currently, stress shielding and the need for secondary surgery are the two major challenges faced by permanent metallic implants. As a new class of biometallic implants with the advantages of high strength, high ductility, and high corrosion resistance at the same time, bulk amorphous alloys (Bulk Metallic Glasses, BMGs) have been proposed as a potential solution to these difficulties. Science is the first report on biomedical metal materials, significant progress has been made. For example, Zberg et al. [12], prepared $Mg_{60+x}Zn_{35-x}Ca_5$ (x=0, 3, 6, 7, 9, 12, 14, and 15) amorphous strips with a thickness of 50 μm via melt spinning and the as-obtained amorphous sheets with a thickness of 0.5mm via copper spray casting. They also demonstrated that $Mg_{60}Zn_{35}Ca_5$ BMG had excellent biocompatibility as it did not cause necrosis or inflammatory symptoms when dissolved in animal cells. Xie et al. [11], implanted cylindrical Mg-Ca-Zn BMGs (Φ0.7 ×5mm) along the axial axis into the distal femorus of 3-month-old C57BL/6 mice, and weekly X-ray and CT examinations were performed to measure material degradation and bone changes around the materials. After 4 weeks, samples were collected and examined. The study found that fragmenting materials stimulated new bone formation around the implant, as Mg-Ca-Zn BMGs degraded in vivo without causing inflammatory reactions around the implant site. Currently, the majority of reports on biodegradable medical amorphous alloys focus on Mg-based BMGs. According to reports [4, 8], Mg-based BMGs have been reported to have poorer GFA than Ca-based BMGs. Cao and his colleagues [1] report explain the limited glass-forming ability (GFA) of Mg-based BMGs while examining Ca-based biodegradable amorphous alloys as a potential alternative. The TPF (The Thermoplastic Forming, TPF) of Mg-base alloy is limited to only 20℃, making it difficult to form and cast thick materials. In contrast, Ca-based BMGs with various compositions (Ca-Mg-Zn ternary system) have been prepared by copper casting with better glass-forming ability. The corrosion behavior of these alloys in a minimum necessary medium (MEM) solution was studied and it was found that the content of Zn strongly influenced the corrosion rate. Specifically, there was a linear relationship between the mass loss of the sample and the content of Zn atom, with higher Zn content leading to lower corrosion rates. The critical thicknesses of

Mg-Zn-Ca BMGs and Ca-Mg-Zn BMGs are shown in Table 1 [4,8,14]. Wang et al. [2] conducted in vitro corrosion behavior, ion release, biocompatibility and in vivo implantation tests on $Ca_{65}Mg_{15}Zn_{20}$ BMGs. The results show that $Ca_{65}Mg_{15}Zn_{20}$ BMG is non-toxic and can stimulate bone tissue healing. When Ca-based BMGs are used as biodegradable bioimplants, they are the most successful low-density BMGs found to date (~2.0 gcc^{-1}) and have Young's modulus values comparable to the modulus of human bone of ~20-30 GPa and shear modulus of ~8-15 GPa. Currently, the application of using Ca-based BMGs as biodegradable biomaterials for implantation is still in the primary research stage, and the research and development of non-toxic, biocompatible, and low-cost alloying element compositions, composition ratios, and understanding of their degradation behaviors will help to give full play to their potential as biodegradable implantable materials.

Table 1 Critical thicknesses of Mg-Zn-Ca BMGs and Ca-Mg-Zn BMGs.

Alloys	Critical thickness/mm
$Mg_{66}Zn_{30}Ca_4$	2.4
$Mg_{67}Zn_{28}Ca_5$	3.0
$Mg_{75}Zn_{20}Ca_5$	3.0
$Mg_{62}Zn_{35}Ca_3$	2.0
$Mg_{63}Zn_{33}Ca_4$	2.0
$Mg_{80}Zn_{15}Ca_5$	3.0
$Ca_{55}Mg_{25}Zn_{20}$	1.0
$Ca_{55}Mg_{20}Zn_{25}$	2.0
$Ca_{60}Mg_{20}Zn_{20}$	4.0
$Ca_{60}Mg_{15}Zn_{25}$	6.0
$Ca_{60}Mg_{17.5}Zn_{22.5}$	10.0

In this work, we propose $Ca_{53+x}Mg_{20}Zn_{27-x}$ (x=0, 2, 4, 6, 8, and 10) near the eutectic point of the Ca-Mg-Zn ternary phase diagram. 3 mm amorphous or amorphous-crystalline composite bar alloys via copper spray casting and analyze the glass-forming ability and corrosion resistance of Ca-Mg-Zn BMGs for different composition ratios and in simulated body fluids

(SBF). We also evaluate the impact of Zn content variation on microstructure and corrosion properties

2. Materials and Methods

2.1. Materials preparation

Alloy bars with a nominal composition of $Ca_{53+x}Mg_{20}Zn_{27-x}$ (x=0, 2, 4, 6, 8, and 10) were prepared by high purity Mg, Zn, and Ca with the purity of 99.99 wt.%. The alloy ingot was remelted three times in a quartz tube by induction melting in a high purity argon atmosphere to ensure good composition uniformity, and then the alloy bars with a diameter of 3 mm and length of 100 mm were prepared by copper mold spray casting. A small amount of each alloy rod was taken and lightly ground into fine chips in a grinding bowl for subsequent characterization.

2.2. Materials characterization

DX-2700 X-ray diffractometer with Cu target Kα radiation within a diffraction angle of 10°-80° with a scanning rate of 1°/min and a step size of 0.02° to determine the structure of the Ca-based BMGs alloy. The thermal behavior of the alloy was conducted on a NETZSCH STA449F3 differential scanning calorimeter up to 500 ℃ with a heating rate of 10 ℃/min under flow-purified argon gas. The thermal field emission scanning electron microscope (SEM, SIGMA 500) was used to observe the surface corrosion morphology and surface particle distribution of the materials. Additionally, the energy-dispersive spectrometer (EDS) was used to analyze the type, content, and distribution of elements on the corroded surface of the sample.

2.3. Electrochemical measurements

The preparation steps for the test samples involved polishing with 2000# sandpaper, ultrasonic cleaning with aqueous ethanol for 3 minutes, and drying. The alloy sheets were held using Pt electrode clips during the corrosion process. The corrosion behavior of alloy human simulated body fluid (SBF) was carried out on a CHI660E electrochemical station at 37 ℃. In

the three-electrode system, the saturated calomel electrode was used as the reference electrode, Pt electrode as the auxiliary electrode, and the as-prepared alloy as the working electrode. The 1000 mL of SBF (8.035g of NaCl, 0.355g of $NaHCO_3$, 0.225g of KCl, 0.231g of $K_2HPO_4 \cdot 3H_2O$, 0.311g of $MgCl_2 \cdot 6H_2O$, 0.292g of $CaCl_2$, 0.072g of Na_2SO_4, and 6.118g of $(HOCH_2)_3CNH_2$) was used as the electrolyte. The strip sample was immersed in SBF at 37 ℃ for electrochemical testing. To measure the open circuit potential (E_{OCP}) of the sample, the scanning potential range of the Tafel curve was determined to be E_{OCP} ± 150 mV with a scanning rate of 5 mV/s.

2.4 Immersion test

The test samples were ultrasonically cleaned with acetone, ethanol, and deionized water. Then, a bar sample with a length of 20 mm was cut and embedded on the surface of the epoxy resin. The ratio of the exposed surface area to the SBF volume in contact was 1 cm^2:13 mL. The sample was placed in the SBF at 37 ℃, and the corrosion time was 270 min.

3. Results

3.1. Microstructure analysis

Figure 1 displays the XRD pattern of a Φ3mm $Ca_{53+x}Mg_{20}Zn_{27-x}$ (x= 0, 2, 4, 6, 8, and 10) alloy bar that was prepared using copper spray casting. The XRD pattern of $Ca_{53+x}Mg_{20}Zn_{27-x}$ (x=0, 2, and 4) alloy bar exhibits typical crystal characteristic peaks, and the precipitation phases are mainly Ca_3Zn and $CaZn_2$. This indicates that the 3 mm of $Ca_{53+x}Mg_{20}Zn_{27-x}$ (x=0, 2, 4) alloy bar is a crystalline material [8]. It is observed that as the Zn content decreases, there are no crystal phases present in the XRD pattern. Only a wide diffraction peak can be noticed, indicating the complete amorphousness of the material. Figure 2 displays the TEM pattern of a Φ3mm $Ca_{53+x}Mg_{20}Zn_{27-x}$ (x=6, 8, and 10). The TEM pattern of $Ca_{53+x}Mg_{20}Zn_{27-x}$ (x=6, 8, and 10) clearly shows that there is no crystal precipitation in the alloy bar, which is complete amorphousness of the material.

The DSC curve in Figure 3 provides valuable insights into the thermal behavior of different Ca-Mg-Zn alloys. It appears that the $Ca_{53}Mg_{20}Zn_{27}$ alloy has a lower amorphous content, which

indicates that most bars in this case have a crystalline structure. However, $Ca_{55}Mg_{20}Zn_{25}$ and $Ca_{57}Mg_{20}Zn_{23}$ alloys contain an amorphous phase, as evident from the obvious glass transition process seen in those alloys. The exothermic reaction caused by crystallization followed by the endothermic reaction caused by melting in these alloys confirms the presence of the amorphous phase, which is indicated by the endothermic peak. In Figure 3(b), the alloys $Ca_{59}Mg_{20}Zn_{21}$, $Ca_{61}Mg_{20}Zn_{19}$, and $Ca_{63}Mg_{20}Zn_{17}$ exhibit one, two, and three exothermic peaks, respectively, indicating that they underwent one, two, and three-phase crystallizations. The temperature values corresponding to these events are specified in Figure 3, T_g refers to the glass transition temperature of the alloy, T_x is the temperature at which the alloy begins to crystallize, T_m is the temperature at which the alloy begins melting, and T_l is the temperature at which the alloy begins to liquefy (Detailed numerical values are presented in Table 2). In this table, ΔT_x ($\Delta T_x = T_x - T_g$) refers to the width of the subcooled liquid zone, and T_{rg} ($T_{rg} = T_g/T_l$) denotes the transition temperature of the reduced glass. The T_{rg} of the $Ca_{53+x}Mg_{20}Zn_{27-x}$(x= 0, 2, 4, 6, 8, and 10) alloy increases from 0.241 for $Ca_{55}Mg_{20}Zn_{25}$ to 0.255 for $Ca_{63}Mg_{20}Zn_{17}$, indicating that when Mg is held constant, the glass-forming ability (GFA) of $Ca_{53+x}Mg_{20}Zn_{27-x}$(x=0,2,4,6,8,10) is improved with the decrease of Zn content and the increase of Ca content. The $Ca_{63}Mg_{20}Zn_{17}$ alloy exhibits the best GFA. For amorphous alloys, the transition from a high-energy amorphous state to a stable crystal state typically corresponds to a significant peak in the heat released during crystallization. According to the DSC curve, the larger the exothermic peak area, the stronger the GFA of the alloy [10]. This is because more heat is released during the transition to an amorphous state, indicating a larger enthalpy of crystallization. Among the $Ca_{53+x}Mg_{20}Zn_{27-x}$ alloys, $Ca_{63}Mg_{20}Zn_{17}$ has the largest exothermic peak area and the best GFA, which is in line with T_{rg} results.

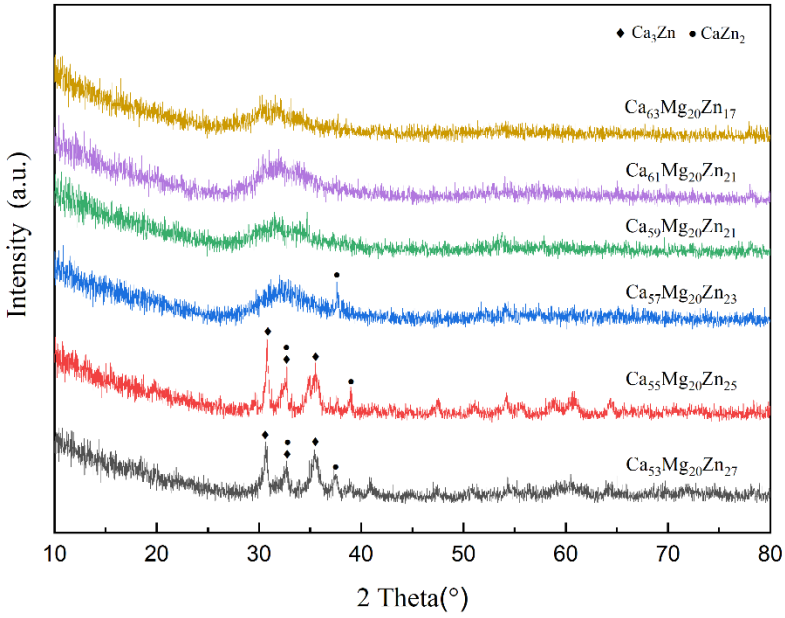

Fig. 1 XRD spectrum of alloy bar with diameter of 3mm $Ca_{53+x}Mg_{20}Zn_{27-x}$(x=0,2,4,6,8,10)

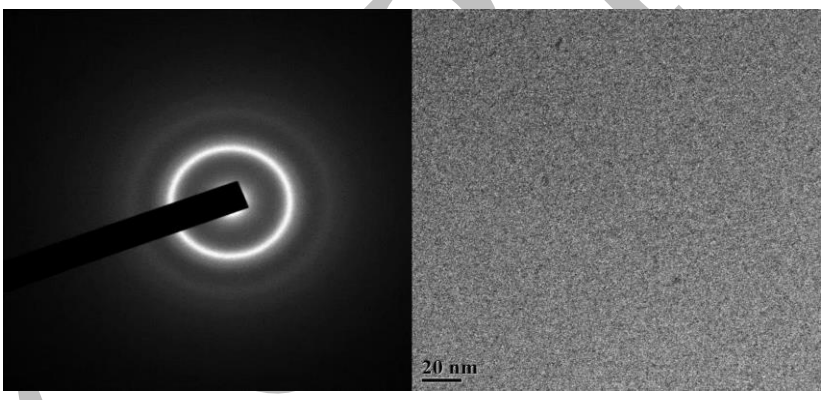

Fig. 2 TEM of alloy bar with diameter of 3mm $Ca_{53+x}Mg_{20}Zn_{27-x}$(x=6,8,and 10)

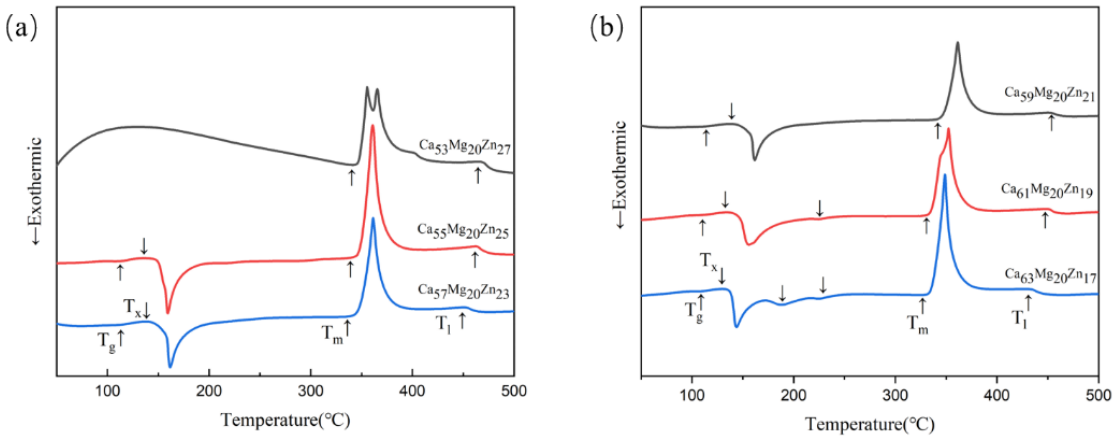

Fig. 3 (a) DSC curve of $Ca_{53+x}Mg_{20}Zn_{27-x}$(x=0,2,4) alloy bar with diameter of 3mm

(b) DSC curve of $Ca_{53+x}Mg_{20}Zn_{27-x}$(x=6,8,10) alloy bar with diameter of 3mm

Table 2 Thermodynamic data of $Ca_{53+x}Mg_{20}Zn_{27-x}$(x=0,2,4,6,8,10) alloy bar with diameter of 3mm

Sample	T_g(℃)	T_x(℃)	T_m(℃)	T_l(℃)	ΔT_x(℃)	T_{rg}(℃/℃)	ΔH(J/g)
$Ca_{53}Mg_{20}Zn_{27}$	/	/	347.4	469.8	/	/	/
$Ca_{55}Mg_{20}Zn_{25}$	113.1	148.6	346.3	469.1	35.5	0.241	41.2
$Ca_{57}Mg_{20}Zn_{23}$	114.9	144.7	346.2	473.1	29.7	0.243	46.0
$Ca_{59}Mg_{20}Zn_{21}$	112.1	146.1	345.8	453.1	34.0	0.247	52.6
$Ca_{61}Mg_{20}Zn_{19}$	111.8	140.2	333.6	449.4	28.4	0.248	72.5
$Ca_{63}Mg_{20}Zn_{17}$	111.1	135.1	333.1	434.5	24.0	0.255	83.0

3.2. Polarization curve measurements

The polarization curve reflects the dynamic interaction between the material and the corrosion system. When the open-circuit potential reaches stability, the corrosion rate can be quantified by the corrosion current density, with lower values indicating slower corrosion rates. Figure 4 shows the dynamic potential polarization curve of both crystalline and amorphous 3 mm $Ca_{53+x}Mg_{20}Zn_{27-x}$ (x= 0, 2, and 4) composite alloy bars in a human simulated body fluid (SBF) at 37 ℃, with the results summarized in Table 3. The open-circuit potential (E_{OCP}) of the $Ca_{53+x}Mg_{20}Zn_{27-x}$ (x=0, 2, and 4) alloy in the SBF at 37 ℃ showed no significant change, indicating equal corrosion tendencies across all three compositions from a thermodynamic perspective. However, kinetic analysis showed that the self-corrosion current density (j_{coor}) of $Ca_{53+x}Mg_{20}Zn_{27-x}$ (x= 0, 2, and 4) composite alloy bars decrease with decreasing Zn content from $6.96\times10^{-4}A\cdot cm^{-2}$ to $4.55\times10^{-4}A\cdot cm^{-2}$, and the self-corrosion potential (E_{coor}) shifting from -1.40V to -1.39V. Thus, the corrosion resistance of the $Ca_{53+x}Mg_{20}Zn_{27-x}$ (x= 0, 2, and 4) composite alloy bars increased with decreasing Zn content. During the electrode reaction process, metal ions in the solution act as charge carriers, responsible for charge transport to the electrode surface. Ca alloy dissolves into metal cations in the cathode region, but the high concentration of metal ions can hinder the charge exchange process, forming an ion cloud obstacle to the electrode. It is generally believed that the larger Rp of the metal, the more effectively the ion cloud on the electrode surface can hinder charge exchange [10]. The Rp of $Ca_{53}Mg_{20}Zn_{27}$ is the smallest, while that of $Ca_{57}Mg_{20}Zn_{23}$ is the largest, indicating an increase

in the corrosion resistance of $Ca_{53+x}Mg_{20}Zn_{27-x}$ (x= 0, 2, and 4) composite alloy bars with decreasing Zn content.

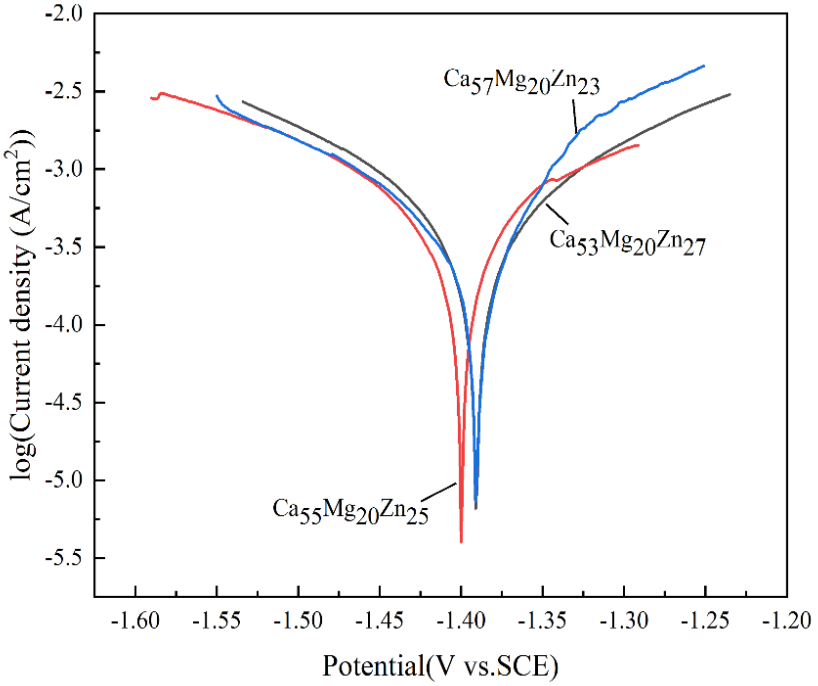

Fig. 4 Polarization curve of $Ca_{53+x}Mg_{20}Zn_{27-x}$(x=0,2,4) composite alloy bar with diameter of 3mm in 37 ℃ simulated body fluid

Table 3 $Ca_{53+x}Mg_{20}Zn_{27-x}$(x=0,2,4) composite alloy bars with a diameter of 3mm Corrosion results in simulated body fluid at 37 ℃

Sample	Rp($\Omega \cdot cm^2$)	E_{OCP} (V)	E_{corr} (V)	j_{corr} ($A \cdot cm^{-2}$)
$Ca_{53}Mg_{20}Zn_{27}$	63.5	-1.38	-1.40	6.96×10^{-4}
$Ca_{55}Mg_{20}Zn_{25}$	63.7	-1.38	-1.39	6.17×10^{-4}
$Ca_{57}Mg_{20}Zn_{23}$	64.5	-1.37	-1.39	4.55×10^{-4}

Figure 5 shows the polarization curves of BMGs bars of Φ3mm in diameter with $Ca_{53+x}Mg_{20}Zn_{27-x}$ (x=6, 8, and 10) compositions. Polarization curve reacts to the kinetic behavior between the material and the corrosion system, in the case of stable open circuit potential, the size of the corrosion current density can reflect the corrosion rate of the faster, the smaller the current density of the alloy corrosion rate is slower. The results of corrosion research are presented in Table 4. The open circuit potential (E_{OCP}) of $Ca_{53+x}Mg_{20}Zn_{27-x}$ (x=6, 8, and 10)

increased from -1.50 V to -1.40 V at 37 ℃, and the most negative E_{OCP} was observed for $Ca_{63}Mg_{20}Zn_{17}$, whereas $Ca_{59}Mg_{20}Zn_{21}$ had the most positive E_{OCP}. Thermodynamic analysis revealed that $Ca_{59}Mg_{20}Zn_{21}$ had a small tendency to corrode, while $Ca_{63}Mg_{20}Zn_{17}$ was more prone to corrosion. Kinetic analysis indicated that the self-corrosion current density of the alloy decreased in the order $Ca_{59}Mg_{20}Zn_{21}$ < $Ca_{61}Mg_{20}Zn_{19}$ < $Ca_{63}Mg_{20}Zn_{17}$, suggesting that as the Zn content decreases in human simulated body fluid (SBF), the corrosion resistance of $Ca_{53+x}Mg_{20}Zn_{27-x}$ (x=6, 8, and 10) BMGs bars deteriorate gradually. Therefore, it can be concluded that the corrosion mechanism of amorphous alloys differs from that of amorphous-crystal composite alloys.

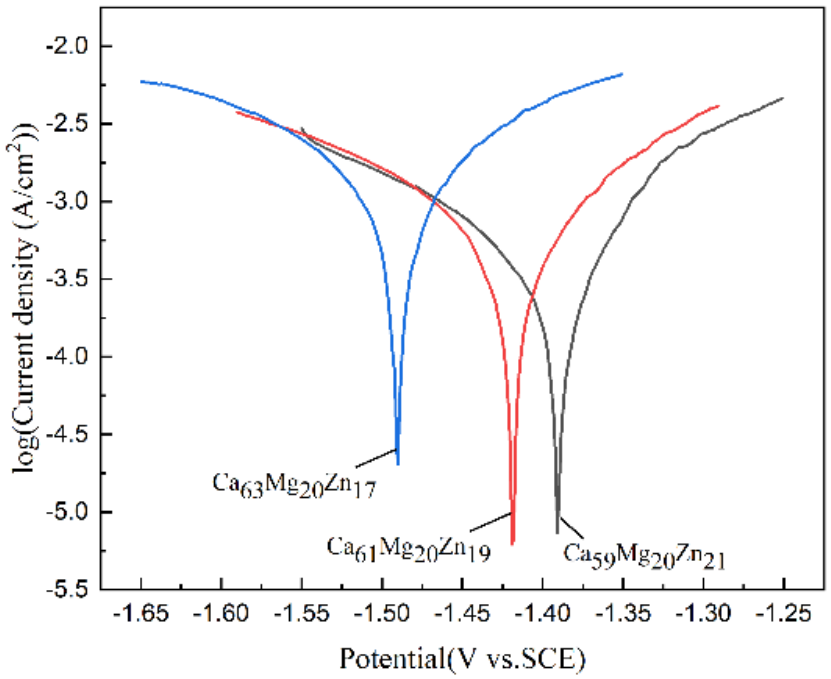

Fig. 5 Polarization Curve of $Ca_{53+x}Mg_{20}Zn_{27-x}$ (x=6,8,10) Amorphous Alloy Bar at 37 ℃ SBF

Table 4 Corrosion Results of $Ca_{53+x}Mg_{20}Zn_{27-x}$ (x=6,8,10) Amorphous Bar with a Diameter of 3mm in 37 ℃ Simulated Body Fluid

Sample	Rp(Ω·cm^2)	E_{OCP} (V)	E_{corr} (V)	j_{corr} (A·cm^{-2})
$Ca_{59}Mg_{20}Zn_{21}$	64.1	-1.40	-1.37	4.68×10^{-4}
$Ca_{61}Mg_{20}Zn_{19}$	49.2	-1.44	-1.41	7.62×10^{-4}
$Ca_{63}Mg_{20}Zn_{17}$	23.4	-1.50	-1.49	1.92×10^{-3}

3.3 Immersion test

Among the completely amorphous alloys, $Ca_{59}Mg_{20}Zn_{21}$ with the slowest degradation rate and $Ca_{63}Mg_{20}Zn_{17}$ with the fastest degradation rate were subjected to corrosion in human simulated body fluid (SBF) at 37 °C for 270 minutes. The surface morphology and element aggregation state of the surface corrosion morphology of $Ca_{59}Mg_{20}Zn_{21}$ alloy bar were characterized and are depicted in Figure 6. The SEM image shows a relatively flat and uniform layer of small particles formed on the surface of the alloy matrix (indicated by the red arrow in the figure) that helped delay the corrosion process and prevent the rapid degradation of the alloy. The corrosion product on the alloy surface appears as irregularly shaped agglomerated polyhedral particles. The parallel shallow gully of about 45° in Figure 6(a) was caused by the sample pretreatment, while the large V-shaped crack was due to dehydration after drying [10]. Figure 6(c) is an enlarged image of region a in Figure 6(a), and the overall topography is similar to that of Figure 6(a). Figure 6(b) displays the local corrosion pits found on the surface of alloy bars, indicating that amorphous Ca-based BMG starts corroding from the local area of the surface and diffuses around because there is no grain boundary for preferential corrosion. Furthermore, EDS analysis revealed the corrosion product of an irregularly aggregated polyhedron particle in Figure 6(a) (point B in Figure 6(c)), and the results are depicted in Figure 6(d). The corrosion products of polyhedral particles were found to contain relatively high amounts of the elements Ca-16.06 at.%, O-69.36 at.% and P-10.87 at.%, while the elements Zn-1.86 at.%, Mg-1.36 at.% and Cl-0.50 at.% were found to contain very little. The Ca/P ratio of the corrosion product, which is 1.47, is similar to the Ca/P ratio of 1.66 of the primary constituent hydroxyapatite ($Ca_{10}(PO_4)_6(OH)_2$) in human bones. Therefore, the corrosion product at point B can be inferred to be ($Ca_{10}(PO_4)_6(OH)_2$).

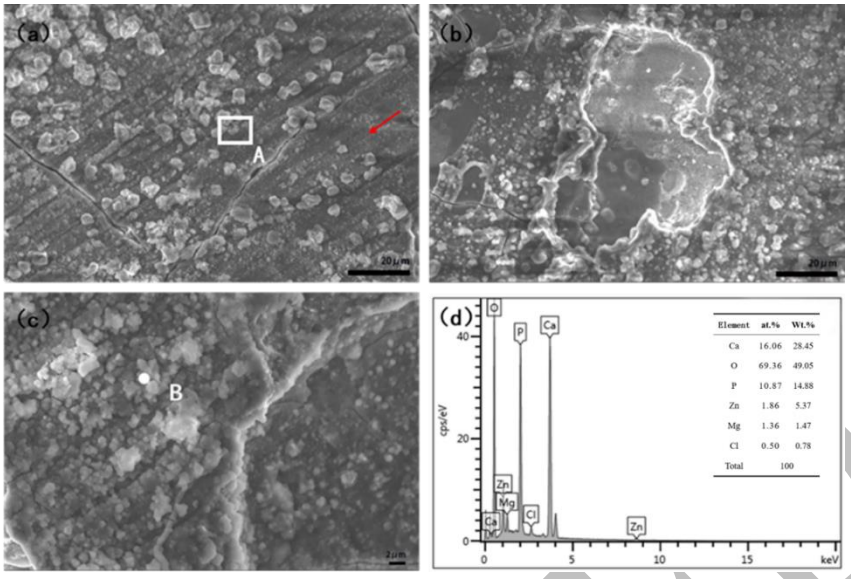

Fig. 6 (a) SEM diagram of surface corrosion morphology of $Ca_{59}Mg_{20}Zn_{21}$ alloy bar after corrosion in SBF, (b)Local corrosion pits on the surface of alloy bars, (c) Enlarged view of area A, (d) EDS analysis diagram of point B

Pitting and uneven corrosion are the most common phenomena observed during the corrosion of magnesium alloys, particularly when exposed to chloride ion-containing solutions [5]. Figure 7 shows the surface corrosion morphology of a $Ca_{63}Mg_{20}Zn_{17}$ alloy bar as analyzed by SEM and EDS. After 270 minutes of corrosion in a simulated human body fluid (SBF) at 37 ℃, a large number of spiral and oblate spherical corrosion products accumulated on the surface of the alloy bar, as shown in points A and B in Figure 7(a). Underneath the majority of the corrosion products is a protective film, which is visible in Figure 7(a) (indicated by the red arrow). It is hypothesized that this initial defensive layer gradually decomposes under the influence of Cl-, resulting in the formation of additional corrosion layers over time, as confirmed by the electrochemical test results. Figure 7(b) displays an enlarged image of region C in Figure 7(a) showing two different corrosion morphologies. EDS analysis was conducted on this region, and the results are shown in Figure 7(1-8): the main elements on the surface of the alloy are O-51.44 at.%, C-20.52 at.%, Ca-11.89 at.%, P-6.08 at.%, Cl-3.21 at.%, Zn-3.73 at.%, and Mg-3.01 at.%, as seen in Figures 7(3) and 7(7).

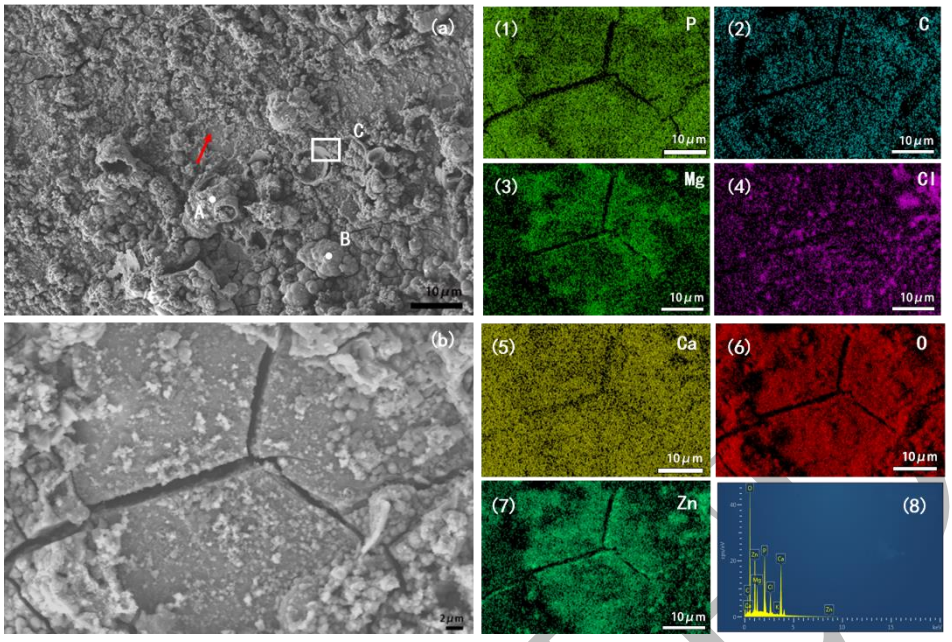

Fig. 7 (a) SEM of surface corrosion morphology of $Ca_{63}Mg_{20}Zn_{17}$ alloy bar after corrosion in SBF, (b) Enlarged view of area C, (1-8) EDS element analysis in area C

3.4 Biocompatibility test

Compliance with biosafety standards is the minimum requirement for determining whether a material can be used as a biological implant material. The cytotoxicity of materials refers to cell death caused by material factors, excluding normal cell metabolism and apoptosis [6]. In vitro studies on $Mg_{60}Ca_5Zn_{35}$, $Mg_{72}Ca_{12}Zn_{16}$, and $Mg_{63}Ca_{15}Zn_{22}$ alloys using MC3T3-E1 cells were conducted by Paul et al. [3] to evaluate their biocompatibility. The results indicated that the cells proliferated in all the alloy extraction media, and after 48 hours of culture, the absorbance (OD) of the cells was similar to that of the control group. Therefore, all the alloys were deemed non-cytotoxic. Figure 8 shows the absorbance value (OD) of MC3T3-E1 cells cultured in $Ca_{53+x}Mg_{20}Zn_{27-x}$ (x=0, 2, 4, 6, 8, and 10) alloy extract for 24 h, 72 h, and 120 h. There was no significant difference in the absorbance value of cells at 24 h, 72 h, and 120 h. However, more live cells were observed growing on the alloy from 24 h to 120 h, and the overall absorbance increased significantly. This finding proved that Ca-Mg-Zn alloy was non-toxic to MC3T3-E1 cells and exhibited good biocompatibility [13].

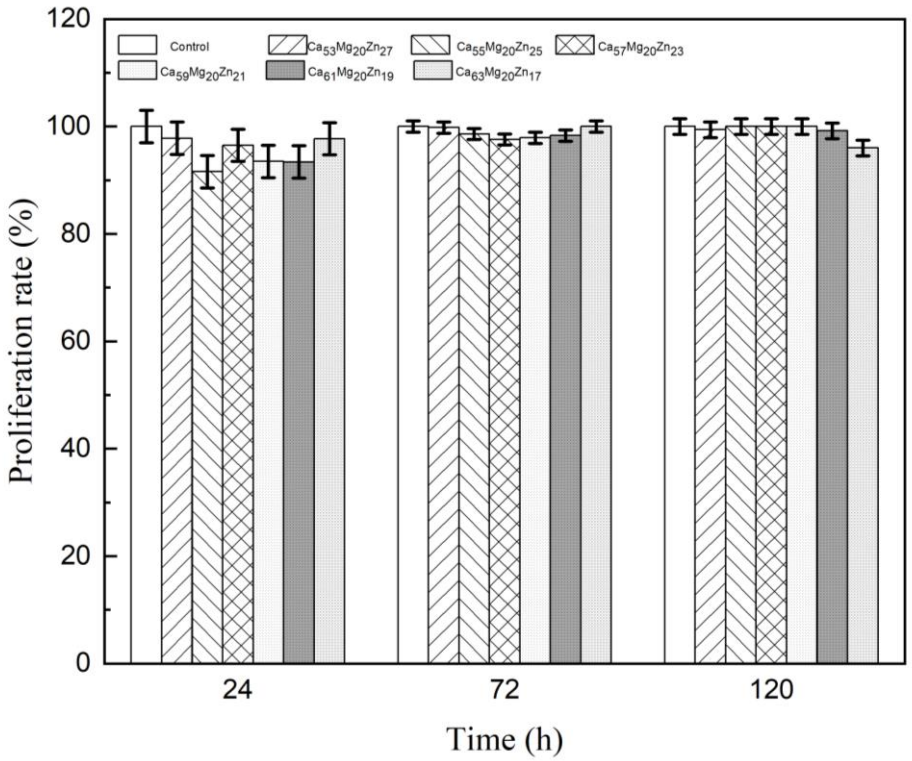

Fig. 8 Diagram of cell OD value after alloy extract culture for different times

4. Discussion

The properties of materials are closely related to their structural organization. As in $Ca_{32}Mg_{12}Zn_{38}Yb_{18-x}B_x$ (x=1,2,3 at.%) alloys, the $Ca_{32}Mg_{12}Zn_{38}Yb_{16}B_2$ was completely amorphous, while a few nanocrystalline grains appeared in $Ca_{32}Mg_{12}Zn_{38}Yb_{17}B_1$ and $Ca_{32}Mg_{12}Zn_{38}Yb_{15}B_3$, and the amount of hydrogen precipitation of $Ca_{32}Mg_{12}Zn_{38}Yb_{18-x}B_x$ (x=1,2,3 at.%) alloys was 0.7, 1.5 and 0.9 ml·cm^{-2}, after 720 h in Ringer's solution [9]. The electrochemical results presented above demonstrate that the corrosion performance of Φ3mm $Ca_{57}Mg_{20}Zn_{23}$ composite bar, containing a small amount of crystal phase, is better than that of a completely amorphous $Ca_{59}Mg_{20}Zn_{21}$ bar. This indicates that the corrosion performance of the alloy is not reduced by the precipitation of a small amount of crystal phase. However, the further increase of the crystal phase leads to reduced corrosion performance [15]. The reason behind this phenomenon is that the volume fraction of crystal phase precipitation is very small, and the crystal phase is surrounded by the amorphous phase. As a result, the corrosion is mainly concentrated in the crystal phase. The crystal phase, acting as the anode, is preferentially

corroded, and the cathode (amorphous matrix) is protected by sacrificing the anode (crystal phase). With further corrosion, the crystal phase is completely corroded off, and more amorphous matrix phases are exposed. The corrosion potential difference between the crystal phase and the substrate disappears, and the galvanic corrosion decreases or disappears. Consequently, the corrosion rate of the alloy decreases, indicating good corrosion resistance. However, when the volume fraction of the precipitated crystal phase is large, the crystal phase in the alloy sample surrounds the amorphous matrix. As the corrosion proceeds, the crystal phase gradually dissolves. This results in the loss of the amorphous matrix and the formation of corrosion pits. Moreover, more alloy is exposed to the corrosive liquid, which further aggravates the corrosion and reduces the corrosion performance of the sample [15].

In a 37°C human simulated body fluid corrosion experiment, the corrosion rate of the completely amorphous $Ca_{63}Mg_{20}Zn_{17}$ alloy is faster than that of the $Ca_{59}Mg_{20}Zn_{21}$ alloy, as the chemical composition has a significant effect on the corrosion behavior of a completely amorphous alloy [7]. This can be observed in the corrosion behavior of both $Ca_{59}Mg_{20}Zn_{21}$ and $Ca_{63}Mg_{20}Zn_{17}$ samples. The corrosion rate of the low-zinc alloy $Ca_{63}Mg_{20}Zn_{17}$ is faster, while the corrosion rate of the zinc-rich alloy $Ca_{59}Mg_{20}Zn_{21}$ is slower. The difference in corrosion behavior of the $Ca_{59}Mg_{20}Zn_{21}$ and $Ca_{63}Mg_{20}Zn_{17}$ alloys can be attributed to the zinc concentration, where a lower zinc content results in worse corrosion resistance. This is the same result as Gao [1] et al in their study of Ca-Mg-Zn BMGs, where the increase in Zn content helped to enhance the corrosion resistance of the alloy.

5. Conclusions

(1) The $Ca_{53+x}Mg_{20}Zn2_{7-x}$ (x= 0, 2, 4, 6, 8, and 10) alloy bars with Φ3 mm are comprised of both crystalline and amorphous composites, where $Ca_{53+x}Mg_{20}Zn_{27-x}$ (x=0, 2, and 4) are crystalline while $Ca_{53+x}Mg_{20}Zn_{27-x}$ (x=6, 8, and 10) are completely amorphous.

(2) At constant Mg, the GFA of $Ca_{53+x}Mg_{20}Zn_{27-x}$ (x=6, 8, and 10) increased with the decrease of Zn content, indicating an increase in Ca content. The $Ca_{63}Mg_{20}Zn_{17}$ alloy had

the best GFA.

(3) In simulated body fluid (SBF) at 37 ℃, the corrosion resistance of $Ca_{53+x}Mg_{20}Zn_{27-x}$ (x=0, 2, and 4) composite alloy bars increase with the decrease of Zn content, while the corrosion resistance of $Ca_{53+x}Mg_{20}Zn_{27-x}$ (x=6, 8, and 10) BMGs bars decrease with the decrease of Zn content. The corrosion performance of $Ca_{57}Mg_{20}Zn_{23}$ composite bar is better than that of the completely amorphous $Ca_{59}Mg_{20}Zn_{21}$ amorphous bar, because a small amount of crystal phase in the amorphous bar acts as anode, protecting the amorphous matrix and improving the corrosion resistance of the system.

(4) The cytotoxicity test shows that Ca-Mg-Zn alloy has good biocompatibility and can be utilized as a biomedical material.

ACKNOWLEDGMENTS

Supported by the National Natural Science Foundation of China (52661001)

Ningxia Hui Autonomous Region Key R&D Program (2023BDE03007)

References

[1] Cao J D, Kirkland N T, Laws K J, et al., Ca-Mg-Zn bulk metallic glasses as bioresorbable metals, J Acta Biomater, 2012, 8(6): 2375-2383, DOI:10.1016/j.actbio.2012.03.009.

[2] Cormac J, Byrne, et al., Materials science. Bulk metallic glasses, J Science, 2008, DOI:10.1126/science.1158864.

[3] CSPA, BPR, CMD, et al., New Mg-Ca-Zn amorphous alloys: Biocompatibility, wettability and mechanical properties-ScienceDirect., J Materialia, 12[2023-12-25], DOI:10.1016/j.mtla.2020.100799.

[4] Li Q F, Weng H R, Suo Z Y, et al., Microstructure and mechanical properties of bulk Mg–Zn–Ca amorphous alloys and amorphous matrix composites, J Materials Science and Engineering: A, 2008, 487(1-2): 301-8, DOI:10.1016/j.msea.2007.10.027.

[5] Li Z, Gu X, Lou S, et al., The development of binary Mg-Ca alloys for use as biodegradable materials within bone, J Biomaterials, 2008, 29(10): 1329-1344, DOI:10.1016/j.biomaterials.2007.12.021

[6] Liu Q S, Study on degradation behavior and mechanical properties of Biocompatible Mg-Zn-Sn-Sr materials, Chongqing University, 2022, DOI:10.27670/d.cnki.gcqdu.2020.001808.

[7] Ramya M, Sarwat S G, Udhayabanu V, et al., Role of partially amorphous structure and alloying elements on the corrosion behavior of Mg–Zn–Ca bulk metallic glass for biomedical applications, J Materials & Design, 2015, 86(DEC.5):829-835, DOI:10.1016/j.matdes.2015.07.154.

[8] Senkov O N, Scott J M, Glass forming ability and thermal stability of ternary Ca–Mg–Zn bulk metallic glasses, J Journal of Non-Crystalline Solids, 2005, 351(37-39):3087-3094, DOI:10.1016/j.jnoncrysol.2005.07.022.

[9] Szyba D, Babilas R, Bajorek A, Structural and electrochemical study of resorbable

$Ca_{32}Mg_{12}Zn_{38}Yb_{18-x}B_x$ (x=1, 2, 3) metallic glasses in Ringer's solution, J Journal of Alloy sand Compounds, 2019, 815:152313, DOI:10.1016/j.jallcom.2019.152313.

[10] Wang J, Ma Y, Guo S, et al., Effect of Sr on the microstructure and biodegradable behavior of Mg–Zn–Ca-Mn alloys for implant application, J Materials & Design, 2018, 153: 308-316, DOI:10.1016/j.matdes.2018.04.062.

[11] Xie X, Wang X, Wang Y, et al., Ca–Mg–Zn metallic glass as degradable biomaterials developed for potential orthopaedic applications, J Bone, 2010, 47(supp-S3): S425-S425, DOI：10.1016/j.bone.2010.09.249.

[12] Zberg B, Uggowitzer P J, Loffler J F, Mg-Zn-Ca glasses without clinically observable hydrogen evolution for biodegradable implants, J Nat Mater, 2009, 8(11), 887–891, DOI:10.1038/nmat2542

[13] Zhang J, Ren L, Yang K, Cytotoxicity of Ti–6Al–4V–5Cu Alloy to MC3T3-E1 Cells, J Acta Metallurgica Sinica (English Letters), 2020, DOI:10.1007/s40195-020-01158-1.

[14] Zhao Y Y，Zhao X，Structural relaxation and its influence on the elastic properties and notch toughness of Mg–Zn–Ca bulk metallic glass，J Journal of Alloys and Compounds, 2012, 515: 154-160， DOI:10.1016/j.jallcom.2011.11.125.

[15] Zhu M L, Preparation and properties of biomedical Mg-Zn-Ca amorphous composites, D Xi 'an Technological University, 2020, DOI:10.27391/d.cnki.gxagu.2019.000180.